

PMSM Control Based on Edge-Field Hall Sensor Signals Through ANF-PLL Processing

Sung-Yoon Jung, *Student Member, IEEE*, and Kwanghee Nam, *Member, IEEE*

Abstract—To detect the rotor angle of the permanent-magnet (PM) synchronous motor (PMSM), two linear Hall sensors are utilized to measure the fringe field of the PM from one end of the rotor. The measured signals look like $\sin \theta$ and $\cos \theta$ but contain large third-order harmonics. To remove the third-order harmonics, an adaptive notch filter (ANF) is utilized. Furthermore, the ANF is closely connected with an orthogonal phase-locked loop (PLL): The ANF eliminates the harmonics from the PLL input, and the PLL output is used for generating the harmonic reference signals that are required by the ANF. That is, the ANF utilizes the PLL outputs in removing the target harmonic components from the PLL inputs. The PLL angle estimates are used for implementing the field-oriented control of a PMSM. Experimental results in the low-speed region look better than the sensorless algorithms. This kind of edge-field detection method is advantageous since it is easy to install and less affected by the stator current, i.e., relatively robust to the armature reaction.

Index Terms—Adaptive notch filter (ANF), linear Hall-effect sensor, permanent-magnet (PM) synchronous motor (PMSM) position sensor, phase-locked loop (PLL).

I. INTRODUCTION

RECENTLY, permanent-magnet (PM) synchronous motors (PMSMs) have been utilized for pumps or compressors for their high power efficiency, high power density with compact size, and easy high-speed operation. However, rotor position monitoring is essential for the field-oriented control of PMSMs. The most common position sensors are absolute encoders and resolvers. However, these sensors are expensive and need extra mechanical coupling structures. In some submerged pumps, the installation of the position sensor can be very difficult.

Lots of sensorless control methods have been developed for PMSMs. They fall into two categories: back electromotive force [1], [2] and signal injection-based methods [3], [4]. The signal injection-based methods work in the low-speed area but generate acoustic noise and suffer secondary saliency and cross-saturation problems [5]–[9]. The cross-saturation effects produce load-dependent position offset, and the secondary saliency that originated from the different spatial harmonics makes the periodical estimation errors. The secondary saliency error is known to be difficult to compensate [5], [6].

Manuscript received July 21, 2010; revised October 25, 2010 and December 5, 2010; accepted December 23, 2010. Date of publication February 17, 2011; date of current version September 7, 2011.

The authors are with the Department of Electronic and Electrical Engineering, Pohang University of Science and Technology (POSTECH), Pohang 790-784, Korea (e-mail: mokona79@postech.ac.kr; kwnam@postech.ac.kr).

Color versions of one or more of the figures in this paper are available online at <http://ieeexplore.ieee.org>.

Digital Object Identifier 10.1109/TIE.2011.2116850

Another area of research is to use Hall sensors for rotor position sensing [10]–[20]. The use of Hall sensors is advantageous because it does not require a mechanical coupling and the cost is low. The brushless dc motor is a typical example, which utilizes discrete hall sensors for rotor position detection. Three Hall sensors produce three phase square waves which are 120° apart. These signals are used for the current commutation. Unfortunately, discrete hall sensors yield very rough position information (60° resolution), so they cannot be used directly for the sinusoidal excitation of the current.

Some researchers have studied the methods of utilizing discrete Hall sensors for the field-oriented control of PMSMs. A position interpolation method within a 60° interval was studied in [10], and an acceleration estimate was used for the rotor angle interpolation [11]. A phase-locked loop (PLL) was utilized for Hall sensor signal processing in [12]. A dual observer was applied to estimate the position and speed [13]. In [14]–[16], sensorless control techniques were hybridized with the Hall sensing method to overcome the weakness of the sensorless control in the low-speed region.

Linear Hall sensors, of course, give better resolution than discrete ones, and they were already applied to position detection in the PMSM drives [17]–[20]. However, linear Hall sensor signals are easily contaminated by many uncertainties: 1) variations in the magnetization of the magnets; 2) positional variation in the Hall sensor mounting; 3) interference from the stator magnetic field (armature reaction); and 4) air-gap field variations due to temperature changes [17]. The distorted Hall sensor signals aggravate the rotor angle estimation accuracy. Therefore, it is difficult to extract accurate position information from linear Hall sensor signals without proper filtering.

In this paper, linear Hall sensors are utilized to detect the axial component of the PM edge field. It is found that the measured Hall signals contain a significant amount of third-order harmonics. Adaptive notch filters (ANFs) are an interesting filter that can be constructed in a closed loop by programming [21]–[23]. The closed-loop transfer function has the same form as the second-order notch filter. Furthermore, the notch frequency is tunable by software, so it is called an ANF. Therefore, it has a great potential to be applicable to electrical systems [24], particularly in motors where the operation frequency changes. The ANF was already used in the power filter [25]–[27].

In this paper, two ANFs were utilized along with an orthogonal PLL to remove the harmonics in the direct and quadrature axes. The ANF outputs were used for canceling out the harmonics in the PLL input, and the PLL output was used for generating the reference harmonic signals for ANFs. This elegant

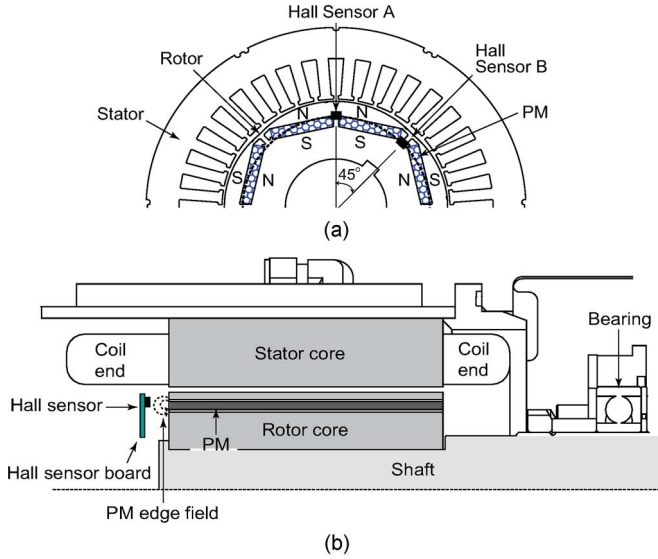


Fig. 1. (a) Cross-sectional and (b) longitudinal views of the PMSM used for experiments.

combination of the ANF and PLL enhances the angle estimation accuracy and contributes to enlarging the PLL bandwidth.

The rest of this paper is organized as follows. First, implementation details for edge-field detection by linear Hall sensors are illustrated. A raw signal processing circuit is also illustrated. Then, the basics of the orthogonal PLL and the ANF are illustrated in Section III. In Section IV, the main idea of incorporating ANFs with the PLL is presented with simulation results. The field-oriented control block diagram for the PMSM is shown in Section V. Finally, experimental results are illustrated.

II. ANGLE ESTIMATION FROM THE PM EDGE FIELD

A. Edge-Field Detection

Fig. 1(a) and (b) shows the cross-sectional view and side view of a PMSM developed for vacuum pumps. It is a four-pole motor, but it has eight cavities for PMs. Two pieces of the PMs constitute a single pole. Note that two Hall sensors are installed at one end of the rotor. Fig. 1(b) shows a longitudinal view of the PMSM along with a Hall sensor that detects the edge field in the axial direction. The two Hall sensors are separated by 45° so that the electrical signals are 90° apart. The sensors are expected to produce sine and cosine waveforms as the rotor turns. The distance from the edge of the PM to the Hall sensor affects the sensor signal level and shape. As the sensor is close to the PM, the signal becomes rectangular due to field saturation. Note that the saturation level of the Hall sensor that we used is ± 0.07 T. On the other hand, as the distance enlarges, the signal shape looks similar to the sinusoidal wave. Based on repeated experimental results, a 5-mm distance was found to be most appropriate. Fig. 2(a) shows the Hall sensors and a signal conditioning circuit mounted on a donut-shaped printed circuit board. Fig. 2(b) shows the printed circuit board after assembly to the motor.

Fig. 3 is a finite-element-method simulation result showing the field vectors at one end of the rotor. The maximum field

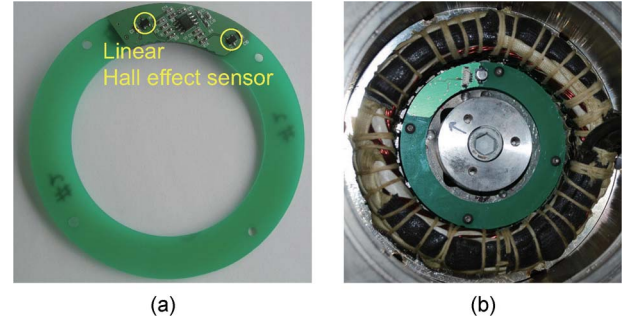


Fig. 2. Hall sensor board and its assembled view: (a) Hall sensor board and (b) assembled view at the end of the rotor.

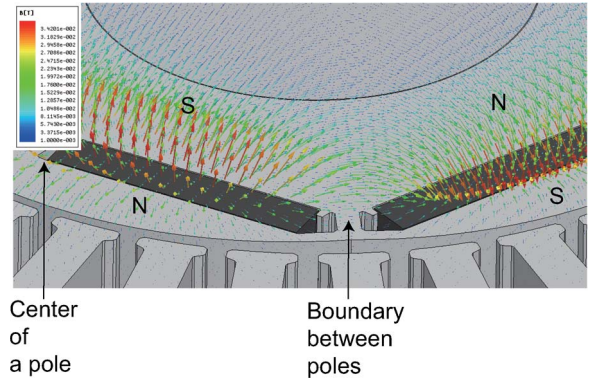


Fig. 3. Edge-field vector distribution (5 mm away from PMs).

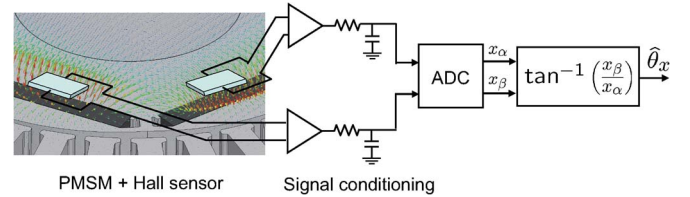


Fig. 4. Hall sensor signal processing procedure for obtaining the rotor angle.

density is calculated as 0.04 T. Note that the axial field components are high around the pole center area. However, the axial component is almost negligible around the pole boundary. Therefore, the axial field density is highest in the pole center and zero in the boundary between the poles.

B. Signal Processing and Angle Estimation

Fig. 4 shows the schematic diagram of the Hall sensor signal processing circuit. The signals are conditioned by low-pass filters. The signals are regarded as sine and cosine functions of the rotor angle. Thus, the rotor angle is calculated as $\hat{\theta}_x = \tan^{-1}(x_\beta/x_\alpha)$.

Fig. 5 shows the experimental results of the Hall sensor signals. The two signals x_α and x_β look similar to sinusoidal waves separated by 90° . Note that a rotor pole consists of two PMs with a gap between them. The gap makes notches on the peak values of x_α and x_β . According to Fourier analysis, the signals contain strong third-order harmonics as shown in Fig. 5(b). The fundamental to the third harmonic ratio is 7.5. Correspondingly, the estimates have errors which can be seen as

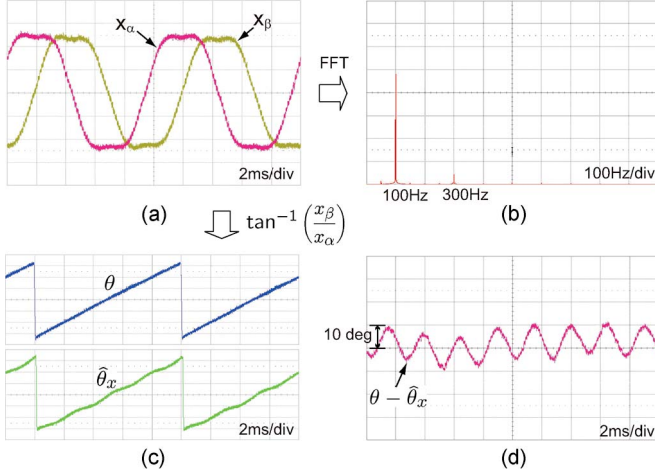


Fig. 5. (a) Raw Hall sensor signals x_α and x_β . (b) FFT of x_α when the rotor rotates at a 100-Hz electrical frequency. (c) Estimated rotor angle $\hat{\theta}_x$ compared with the real one, with θ obtained from an encoder. (d) Angle estimation error.

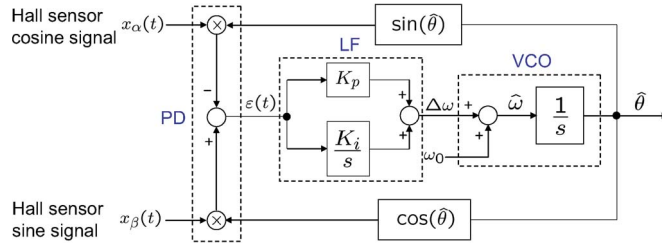


Fig. 6. Application of the orthogonal PLL to motor control.

the deviation from the straight line shown in Fig. 5(c) and (d). The real angle θ was obtained from an encoder.

III. POST SIGNAL PROCESSING BY ORTHOGONAL PLL AND ANF

In the PMSM application, the raw estimate $\hat{\theta}$ is hardly used since it contains large errors that originated from Hall sensor signal harmonics. In the post processing, two processing techniques are applied: PLL and ANF.

A. PLL

The PLL is used to synchronize the output signal with the input signal in frequency as well as in phase [28]. The PLL is basically a tracking filter equipped with a proportional–integral controller which forces an internally generated sinusoidal wave to track the input signal. The use of the PLL in the motor application is beneficial since it filters out harmonics and provides angle along with speed information.

Fig. 6 shows a block diagram of an orthogonal PLL which could be used for motor or ac/dc converter applications. In the normal PLL, the frequency is fixed. However, in motor control applications, the base frequency changes along with the motor speeds. The orthogonal PLL is suitable for processing an orthogonal pair, and its performance is obviously better than the normal PLL that handles a single stream. Hall sensor measurements x_α and x_β are applied to the orthogonal PLL as inputs. Note that $\varepsilon(t)$ is called the phase detector (PD) output

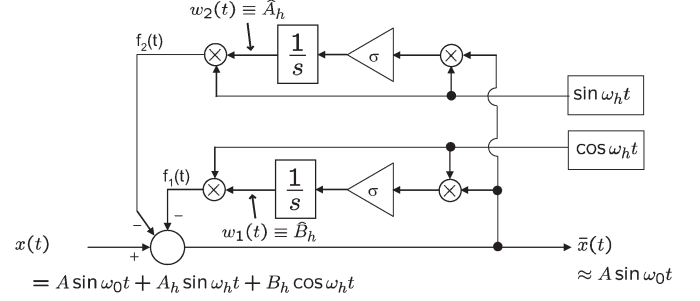


Fig. 7. Functional block diagram of the ANF.

[28]. In the normal PLL, the second-order harmonic appears as a result of multiplying sine and cosine functions [29]. It should be filtered out by the loop filter (LF). However, in the orthogonal PLL, the second-order harmonic is not present, which alleviates the problem of selecting the LF gains.

Even in the orthogonal PLL, the effects of harmonics higher than the second order still remain. Suppose that the input signals contain third-order harmonics such that

$$\begin{aligned} x_{\alpha 0}(t) &= A \sin \left(\omega_0 t + \frac{\pi}{2} \right) + A_h \sin \left(3\omega_0 t + \frac{3\pi}{2} \right) \\ &= A \cos \omega_0 t - A_h \cos 3\omega_0 t \\ x_{\beta 0}(t) &= A \sin \omega_0 t + A_h \sin 3\omega_0 t \end{aligned} \quad (1)$$

where $x_{\alpha 0}(t)$ and $x_{\beta 0}(t)$ are the quadrature inputs, ω_0 is the fundamental frequency of the input signal, and A and A_h are the amplitudes of the fundamental and harmonic components, respectively. Then, $\varepsilon(t)$ is equal to

$$\begin{aligned} \varepsilon(t) &= x_{\beta 0}(t) \cos \hat{\omega} t - x_{\alpha 0}(t) \sin \hat{\omega} t \\ &= A \sin ((\omega_0 - \hat{\omega})t) + A_h \sin ((3\omega_0 + \hat{\omega})t). \end{aligned} \quad (2)$$

Assuming that $\omega_0 \approx \hat{\omega}$, then $\varepsilon(t)$ contains fourth-order harmonics. This causes the LF bandwidth to be small so that the transient response deteriorates [30]. This problem becomes severe in the low-speed region. Therefore, it is necessary to remove the third-order harmonics before applying to the PLL.

B. ANF

As discussed earlier, the PLL bandwidth can be enlarged as the input signals have less harmonics. The harmonics can be filtered out by a notch filter. The ANF is a notch filter that is constructed by a closed loop [21], [22], [29] as shown in Fig. 7. It is assumed that a desired signal $A \sin \omega_0 t$ is mixed with direct and quadrature high-order harmonics $A_h \sin \omega_h t$ and $B_h \cos \omega_h t$.

Two feedback loops are required for $\sin \omega_h t$ and $\cos \omega_h t$. Hereforth, only the $\cos \omega_h t$ loop is discussed since the same is applicable for $\sin \omega_h t$. We let $W_1(s) \equiv \mathcal{L}(w_1)$ and $\bar{X}(s) \equiv \mathcal{L}(\bar{x})$, where \mathcal{L} is a Laplace operator. Note that

$$\begin{aligned} W_1(s) &= \mathcal{L} \left[\int \left(\bar{x}(t) \cdot \frac{\sigma}{2} (e^{j\omega_h t} + e^{-j\omega_h t}) \right) dt \right] \\ &= \frac{\sigma}{2s} \cdot \{ \bar{X}(s + j\omega_h) + \bar{X}(s - j\omega_h) \}. \end{aligned}$$

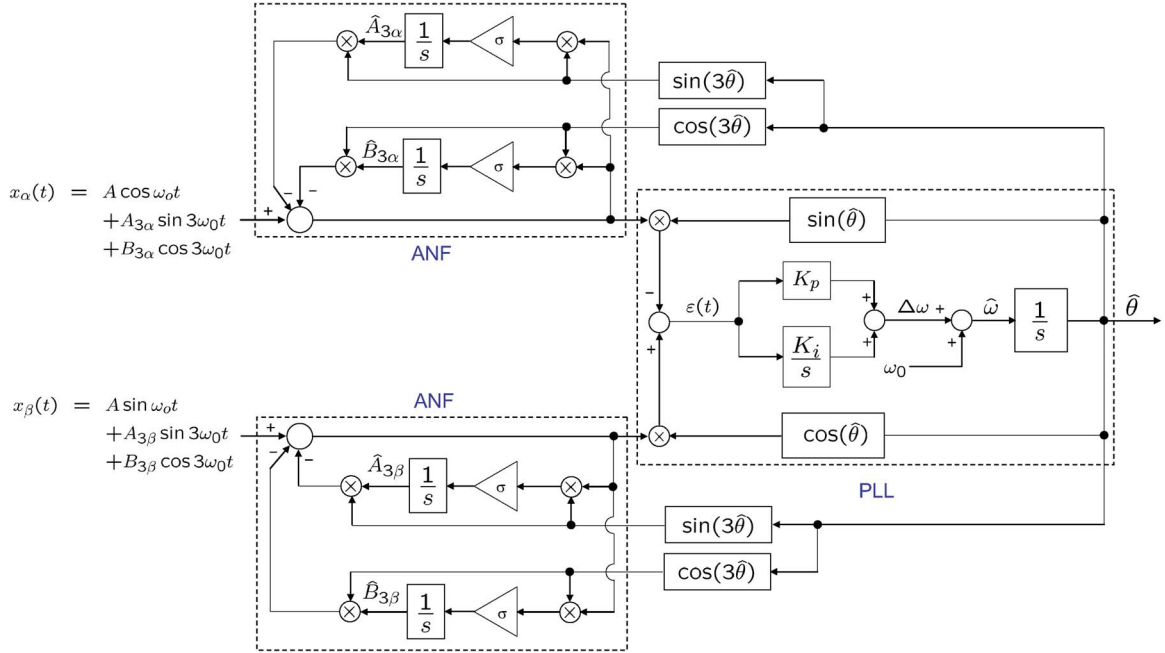


Fig. 8. Proposed Hall sensor signal processing block incorporating the orthogonal PLL with the ANF.

Since $f_1(t) = w_1(t) \times \cos \omega_h t$, the Laplace transform of $f_1(t)$ is equal to

$$\begin{aligned} F_1(s) &= \frac{1}{2} \cdot \{W_1(s + j\omega_h) + W_1(s - j\omega_h)\} \\ &= \frac{\sigma}{4(s + j\omega_h)} \{\bar{X}(s) + \bar{X}(s + 2j\omega_h)\} \\ &\quad + \frac{\sigma}{4(s - j\omega_h)} \{\bar{X}(s) + \bar{X}(s - 2j\omega_h)\}. \end{aligned}$$

Similarly, a Laplace transform of $f_2(t)$ is

$$\begin{aligned} F_2(s) &= \frac{\sigma}{4(s + j\omega_h)} \{\bar{X}(s) - \bar{X}(s + 2j\omega_h)\} \\ &\quad + \frac{\sigma}{4(s - j\omega_h)} \{\bar{X}(s) - \bar{X}(s - 2j\omega_h)\}. \end{aligned}$$

Note that

$$\bar{X}(s) = X(s) - F_1(s) - F_2(s) = X(s) - \frac{\sigma s}{s^2 + \omega_h^2} \cdot \bar{X}(s). \quad (3)$$

Therefore, the closed-loop transfer function of the ANF is

$$H(s) \equiv \frac{\bar{X}(s)}{X(s)} = \frac{s^2 + \omega_h^2}{s^2 + \sigma s + \omega_h^2}. \quad (4)$$

Equation (4) is exactly the same as the conventional second-order notch filter: Its gain is zero at $s = j\omega_h$ and almost unity at $s \neq j\omega_h$. Thus, the harmonic components of ω_h are filtered out. Note that the Q -factor is the inverse of σ , and it determines the sharpness of a notch filter. It should be noted from (3), (4), and Fig. 7 that w_1 and w_2 are the estimates of the harmonic coefficients B_h and A_h , respectively. Therefore, they are denoted as $w_1 \equiv \hat{B}_h$ and $w_2 \equiv \hat{A}_h$.

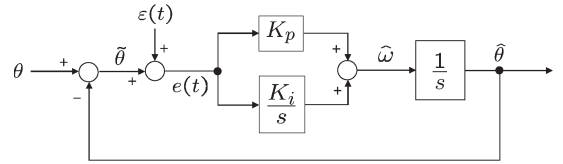


Fig. 9. Linearized PLL block diagram.

IV. PLL INCORPORATING ANF

Fig. 8 shows the proposed signal processing block diagram incorporating the orthogonal PLL with the ANF. Since the two Hall sensor signals x_α and x_β have large third-order harmonics, they can be modeled as

$$\begin{aligned} x_\alpha &= A \cos \omega_0 t + A_{3\alpha} \sin 3\omega_0 t + B_{3\alpha} \cos 3\omega_0 t, \\ x_\beta &= A \sin \omega_0 t + A_{3\beta} \sin 3\omega_0 t + B_{3\beta} \cos 3\omega_0 t. \end{aligned}$$

Thus, two ANFs are employed to filter out the third harmonic components. Obviously, the ANFs are the prefilters located at the upstream of an orthogonal PLL. As was already discussed in the previous section, prefiltering is helpful in enlarging the PLL bandwidth.

Recall from Fig. 7 that harmonic reference signals $\sin \omega_h t$ and $\cos \omega_h t$ are necessary to activate the ANFs. Note, however, from Fig. 8 that there are two feedback paths from the PLL to the ANFs that return $\cos 3\hat{\theta}$ and $\sin 3\hat{\theta}$. That is, the reference signals are generated naturally with the use of angle estimate $\hat{\theta}$ which is available from the PLL output.

A. Linearized Model of the PLL

We regard the remaining or uneliminated harmonics as a disturbance to the PLL system and denote it by $\varepsilon(t)$. Applying linearization to (2) and slightly abusing the notation, we let $e(t) = \varepsilon(t) + \hat{\theta}(t)$, where $\hat{\theta} = \theta - \hat{\theta}$.

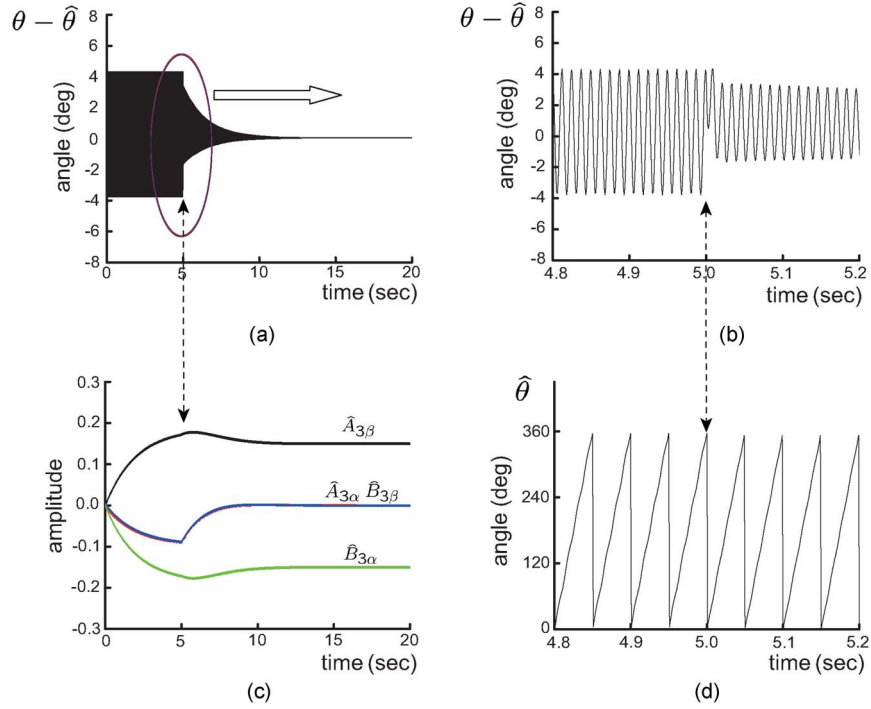


Fig. 10. Simulation results of the proposed scheme at 20 Hz. (a) Angle estimation error. (b) Magnified plot of (a) around $t = 5$ s. (c) Estimates of the third-order harmonic coefficients. (d) Angle estimate around $t = 5$ s.

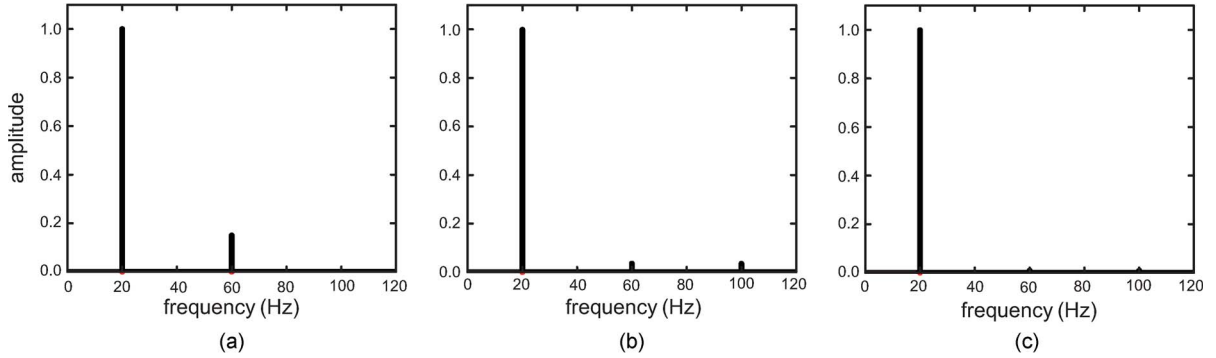


Fig. 11. FFTs of (a) input signal x_β , $S/N = 16.5$ dB, (b) $\sin \hat{\theta}$ with only PLL, $S/N = 36.6$ dB, and (c) $\sin \hat{\theta}$ with PLL plus ANF, $S/N = 48.7$ dB.

Then, we have the linearized PLL dynamics shown in Fig. 9, and the transfer function from $\varepsilon(t)$ to $\hat{\theta}(t)$ is equal to

$$H_p(s) = \frac{\hat{\theta}}{\varepsilon} = -\frac{K_p s + K_i}{s^2 + K_p s + K_i}.$$

The poles are selected to have equal roots such that $H_p(s) = -(2\rho s + \rho^2)/(s + \rho)^2$ like in [30].

Now, the problem is reduced to selecting ρ . Note that the bandwidth of $H_p(s)$ is 2.48ρ . In the previous section, it was shown that uneliminated or residual third-order harmonic components made fourth-order harmonics in the PLL. To attenuate the fourth-order harmonic, the bandwidth of $H_p(s)$ should be less than $4\omega_0$. However, if the loop bandwidth is too small, the PLL causes a large phase delay. Therefore, harmonic filtering and fast tracking ability should be traded off. Giving some margin, we choose ρ such that $4\omega_0 > 4\rho$. Note that $|H(j4\rho)| = 0.47$.

B. Simulations

To demonstrate the performance of the proposed scheme, a simulation study was conducted using MATLAB/SIMULINK. We let $\sigma = 1$, $x_\alpha = \cos(40\pi t) - 0.15 \cos(120\pi t)$, and $x_\beta = \sin(40\pi t) + 0.15 \sin(120\pi t)$. The fundamental to the third-order harmonic amplitude ratio was set to 1 : 0.15.

Fig. 10 shows $\hat{\theta}$, $\theta - \hat{\theta}$, $\hat{A}_{3\alpha}$, $\hat{B}_{3\alpha}$, $\hat{A}_{3\beta}$, and $\hat{B}_{3\beta}$ with and without ANFs. Initially, the ANFs were disabled. After $t = 5$ s, the ANFs start to operate along with the PLL. The time when the ANFs start to operate is marked by the vertical arrows. Fig. 10(a) shows that the initial angle error vanishes as soon as the ANFs are turned on. Fig. 10(b) is a magnified error plot around $t = 5$ s. Note from Fig. 10(b) that the error carries the fourth-order component as described in (2). Fig. 10(c) shows the converging behavior of the ANF parameters to the real harmonic coefficients, i.e., $\hat{A}_{3\alpha} \rightarrow A_{3\alpha} = 0$, $\hat{B}_{3\alpha} \rightarrow B_{3\alpha} = -0.15$, $\hat{A}_{3\beta} \rightarrow A_{3\beta} = 0.15$, and $\hat{B}_{3\beta} \rightarrow B_{3\beta} = 0.0$. Fig. 11 is an extension of Fig. 10, showing a combined performance of

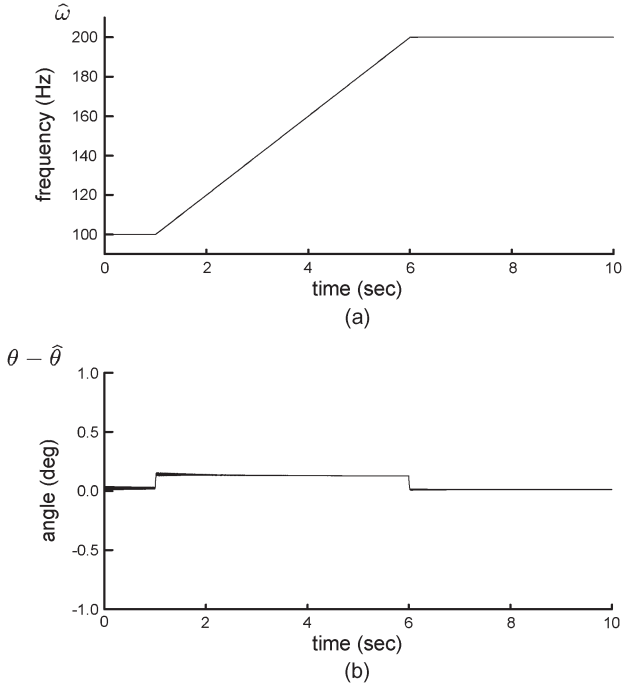


Fig. 12. Simulation results of the proposed ANF-PLL processing scheme as the operation frequency changes from 100 to 200 Hz. (a) Estimated speed. (b) Angle estimation error.

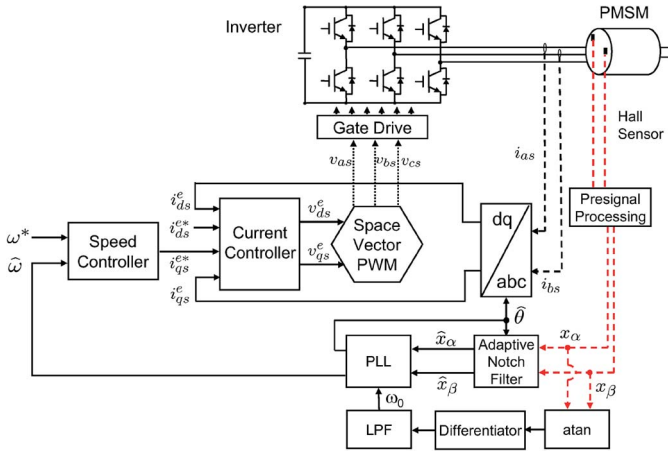


Fig. 13. Overall PMSM control block based on the ANF-PLL filtering.

the ANF and PLL in the spectral domain. Note that the third-order harmonics disappeared completely after the ANFs were activated.

Fig. 12 shows the transient performance when the operation frequency changes from 100 to 200 Hz. The PLL closed loop has double poles at -250 . It shows that the angle error takes place when the operation frequency changes, but its magnitude is quite small (0.2°) from the motor control viewpoint.

V. FIELD-ORIENTED CONTROL BASED ON HALL POSITION SENSORS

Fig. 13 shows the speed control block diagram of the PMSM that utilizes the proposed position sensing scheme. The position sensing scheme consists of edge-field-detecting Hall sensors, a presignal processing circuit, an ANF, and a PLL. The PLL

TABLE I
PMSM PARAMETERS

Variable	Value	Variable	Value
No. of poles	4	Speed (rated)	6000 rpm
Power (rated)	10.0 kW	Voltage (rated, line-to-line)	380 V (rms)
Current (rated)	17.6 A (rms)	Torque	16.0 Nm
D-axis ind.	2.7mH	Q-axis ind.	4.5mH

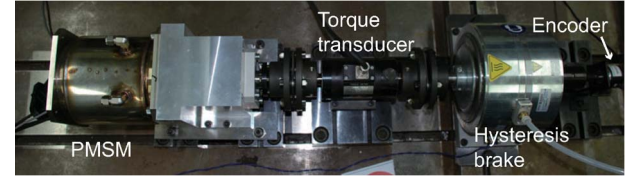


Fig. 14. Experimental setup consisting of PMSM, torque transducer, hysteresis brake, and encoder.

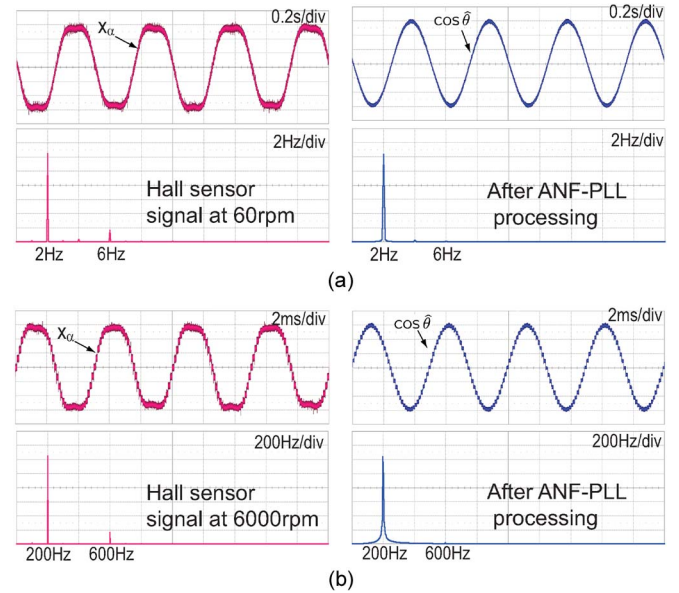


Fig. 15. Hall sensor signals and their FFT before and after the proposed signal processing. (a) 60 r/min (0.01 p.u.). (b) 6000 r/min (1 p.u.).

outputs an angle estimate $\hat{\theta}$ which is used for the field-oriented control. Note that $\hat{\theta}$ is used in the ANF, forming a closed loop. An option is to use ω_0 obtained from differentiating $\tan^{-1}(x_\beta/x_\alpha)$. Since the integral controller in the PLL takes care of the dc offset, one may not use ω_0 .

According to the field-oriented control scheme, the current control is established in the synchronous frame. In the current controller, the maximum-torque-per-ampere control is used within the base-speed region. Above the base speed, the general field weakening control is used.

VI. EXPERIMENTAL RESULTS

Table I shows the PMSM parameters used in this experiment.

Fig. 14 shows a photograph of the experimental setup consisting of a PMSM, a torque transducer, a hysteresis brake, and an encoder.

Fig. 15 shows the time plots and the fast Fourier transforms (FFTs) of Hall sensor signals before and after signal processing. It is an experimental verification that the ANF PLL removes

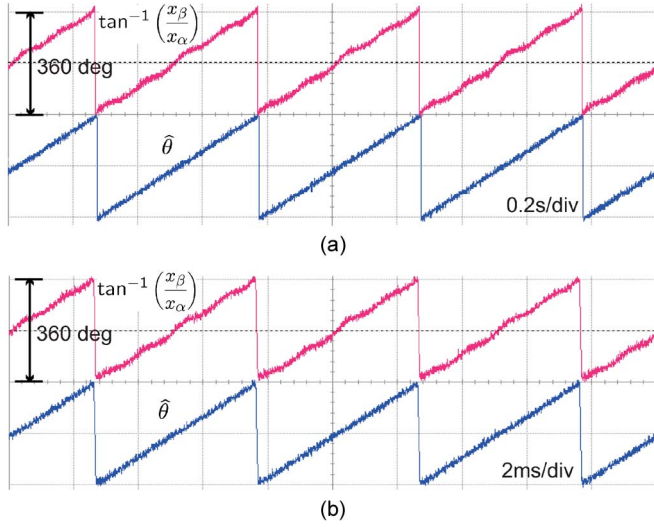


Fig. 16. Rotor angle before and after the proposed signal processing. (a) At 60 r/min (0.01 p.u.). (b) At 6000 r/min (1 p.u.).

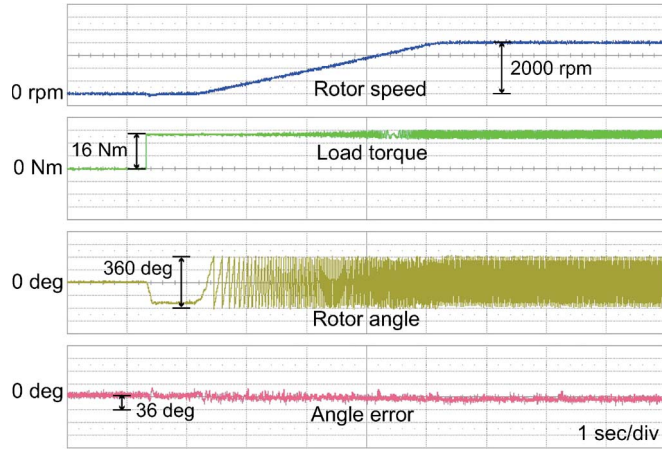


Fig. 17. Start-up from standstill to 2000 r/min with 100% load.

the third-order harmonics effectively at both low and high speeds. Note, however, that the PLL gains were set differently: Closed-loop poles of the PLL were set at -50 for low-speed operation and at -100 for high-speed operation. In both cases, σ was fixed at 2.0. Fig. 16 shows the corresponding angle estimates to the signals shown in Fig. 15. Obviously, linearity in $\hat{\theta}$ is an indication of harmonic removal.

Figs. 17 and 18 show the performance during start-up with a 100% load. The two results were obtained under the same condition. However, the first figure shows that the angle error was bounded in the whole accelerating region, and the second figure shows the converging behavior of the harmonic estimates, i.e., it shows that $\hat{A}_{3\beta} \rightarrow 0.031$ and $\hat{B}_{3\alpha} \rightarrow -0.032$. The converging profiles are similar to those of the simulation results shown in Fig. 10. It took about 3 s for the estimates to converge (in engineering sense).

Fig. 19 shows the speed regulation performance at 6000 r/min. A step load of 13.4 N·m was applied under no load condition. The peak angle error was 8°.

However, a big concern is the low-speed performance. Recall that the PLL pole is selected as $\rho < \omega_0$, which means that the

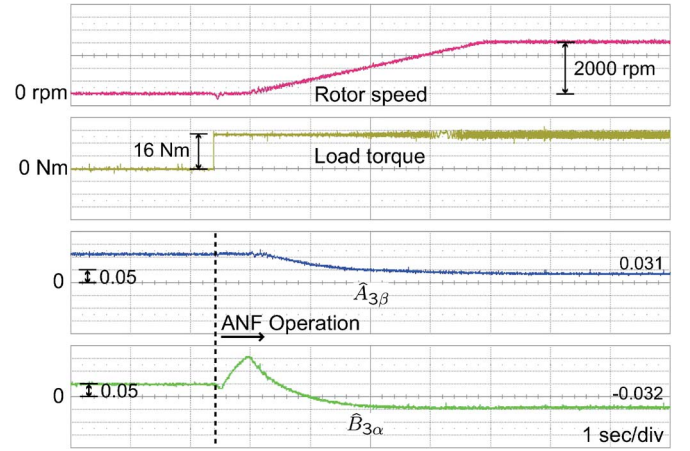


Fig. 18. Convergence of third harmonic coefficient estimates during acceleration.

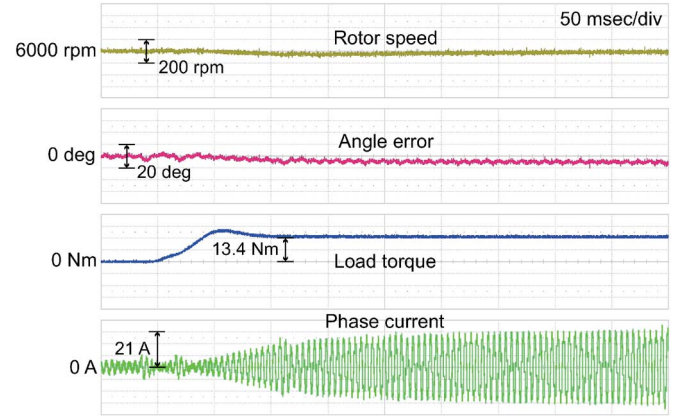


Fig. 19. Speed response under 84% load at 6000 r/min (1 p.u.).

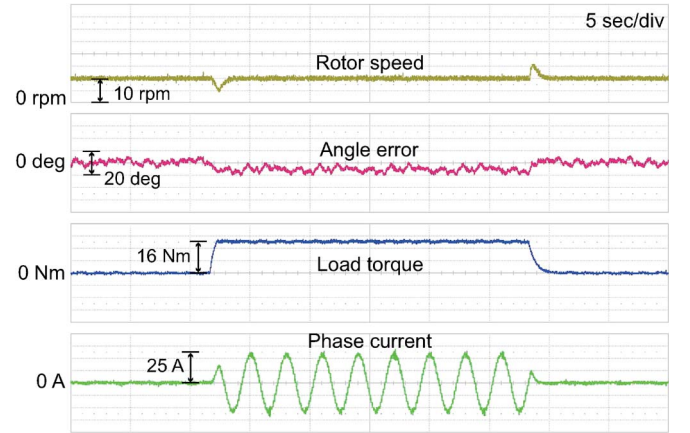


Fig. 20. Speed response under 100% load at 10 r/min (0.0016 p.u.).

PLL bandwidth becomes small as the speed decreases. It causes a big delay, making the system unstable. Thus, we utilized a fixed gain in the low-speed region (0–300 r/min).

To see the low-speed performance, a test was done at 10 r/min. Fig. 20 shows a speed regulation performance at 10 r/min. A full load (16 N·m) was applied in a step manner. The performance looked acceptable, and the angle error was limited below 10°.

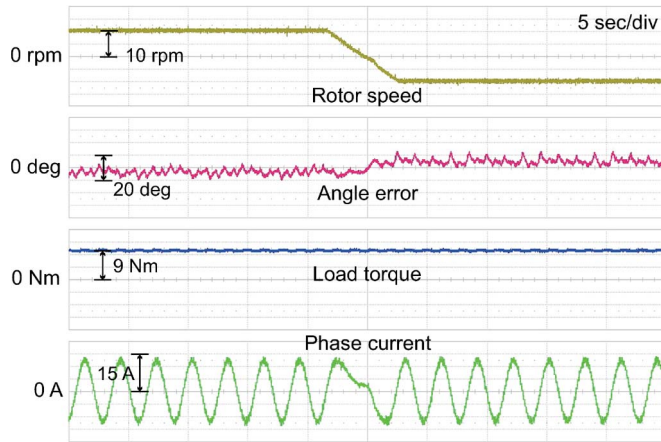


Fig. 21. Speed control performance near zero speed under 56% load.

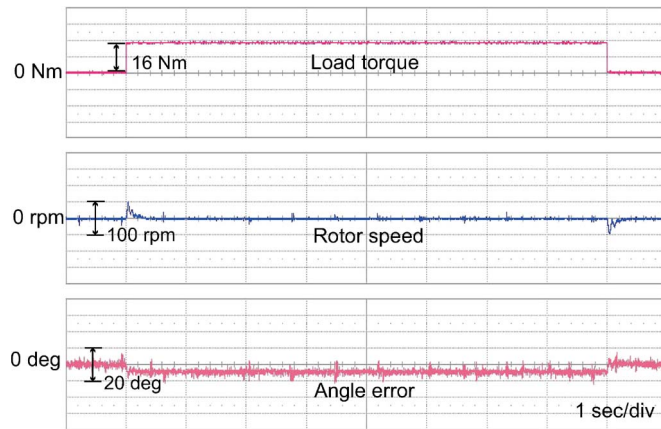


Fig. 22. Zero-speed control performance under 100% step load.

Fig. 21 shows the speed reversal performance. The PMSM was accelerated from 10 to -10 r/min with a 56% load. At 0 r/min, the rotating direction was changed after a brief hesitation. This is because the hysteresis brake always applies a load to the PMSM in the opposite direction. Note that the estimation error was kept nearly zero during (speed) zero crossing.

Fig. 22 shows the zero-speed control performance under a 100% step load. The maximum speed error was 50 r/min, and the angle estimation error was bounded within 10° . For the zero-speed experiments, the hysteresis brake was replaced by a load motor (another PMSM). According to past experimental records, most signal injection sensorless schemes yielded about 50° error in the low-speed region [6], [9], [31]. Based on this fact, the proposed ANF-PLL method seems to show better performance than the sensorless control schemes.

VII. CONCLUSION

Linear Hall sensors are utilized as a low-cost position sensor for PMSMs. Two Hall sensors are positioned on the end of a rotor to detect the axial component of the PMs in the rotor. Therefore, they are less affected by the stator current (armature reaction). The monitored signals contain large third-order harmonics. Two ANFs are utilized to remove both the direct and quadrature components of the third-order harmonics. The

filtered signals are fed to an orthogonal PLL. On the other hand, the angle estimate of the PLL is used to run the ANFs. With this synergetic combination, the filtering performance was enhanced.

A PMSM control loop was constructed based on the ANF-PLL filter, and its performances were demonstrated through simulations and experiments. Apart from the high-speed operation (6000 r/min), the proposed scheme performed satisfactorily at 0 r/min with a full load. Furthermore, it does not show any problem in speed reversal. However, the disadvantage of the edge-field method is that it requires sensor cabling and a small Hall sensor board, although being small. Therefore, the proposed method is suitable for the applications in which the motor and inverter box are assembled in a single unit. Finally, the proposed scheme can be extended easily to the signals containing multiple high-order harmonics.

REFERENCES

- [1] F. Genduso, R. Miceli, C. Rando, and G. R. Galluzzo, "Back EMF sensorless-control algorithm for high-dynamic performance PMSM," *IEEE Trans. Ind. Electron.*, vol. 57, no. 6, pp. 2092–2100, Jun. 2010.
- [2] K. Raggl, B. Warberger, T. Nussbaumer, S. Burger, and J. W. Kolar, "Robust angle-sensorless control of a PMSM bearingless pump," *IEEE Trans. Ind. Electron.*, vol. 56, no. 6, pp. 2076–2085, Jun. 2009.
- [3] F. Cupertino, P. Giangrande, G. Pellegrino, and L. Salvatore, "End effects in linear tubular motors and compensated position sensorless control based on pulsating voltage injection," *IEEE Trans. Ind. Electron.*, vol. 58, no. 2, pp. 494–502, Feb. 2011.
- [4] S. Sayeef, G. Foo, and M. F. Rahman, "Rotor position and speed estimation of a variable structure direct-torque-controlled IPM synchronous motor drive at very low speeds including standstill," *IEEE Trans. Ind. Electron.*, vol. 57, no. 11, pp. 3715–3723, Nov. 2010.
- [5] H. W. De Kock, M. J. Kamper, and R. M. Kennel, "Anisotropy comparison of reluctance and PM synchronous machines for position sensorless control using HF carrier injection," *IEEE Trans. Power Electron.*, vol. 24, no. 8, pp. 1905–1913, Aug. 2009.
- [6] D. Raca, P. Garcia, D. Reigosa, F. Briz, and R. Lorenz, "A comparative analysis of pulsating vs. rotating vector carrier signal injection-based sensorless control," in *Proc. IEEE Appl. Power Electron. Conf.*, Feb. 2008, pp. 879–885.
- [7] C. Silva, G. M. Asher, and M. Sumner, "Hybrid rotor position observer for wide speed-range sensorless PM motor drives including zero speed," *IEEE Trans. Ind. Electron.*, vol. 53, no. 2, pp. 373–378, Apr. 2006.
- [8] P. Guglielmi, M. Pastorelli, and A. Vagati, "Impact of cross-saturation in sensorless control of transverse-laminated synchronous reluctance motors," *IEEE Trans. Ind. Electron.*, vol. 53, no. 2, pp. 429–439, Apr. 2006.
- [9] N. Imai, S. Morimoto, M. Sanada, and Y. Takeda, "Influence of magnetic saturation on sensorless control for interior permanent-magnet synchronous motors with concentrated windings," *IEEE Trans. Ind. Appl.*, vol. 42, no. 5, pp. 1193–1200, Sep./Oct. 2006.
- [10] S. Morimoto, M. Sanada, and Y. Takeda, "Sinusoidal current drive system of permanent magnet synchronous motor with low resolution position sensor," in *Conf. Rec. IEEE IAS Annu. Meeting*, Oct. 1996, pp. 9–14.
- [11] S. B. Ozturk, B. Akin, H. A. Toliyat, and F. Ashrafzadeh, "Low-cost direct torque control of permanent magnet synchronous motor using Hall-effect sensors," in *Proc. IEEE Appl. Power Electron. Conf.*, Mar. 2006, pp. 19–23.
- [12] F. G. Capponi, G. De Donato, L. Del Ferraro, O. Honorati, M. C. Harke, and R. D. Lorenz, "AC brushless drive with low-resolution Hall-effect sensors for surface-mounted PM machines," *IEEE Trans. Ind. Appl.*, vol. 42, no. 2, pp. 526–535, Mar./Apr. 2006.
- [13] A. Yoo, S.-K. Sul, D.-C. Lee, and C.-S. Jun, "Novel speed and rotor position estimation strategy using a dual observer for low resolution position sensors," *IEEE Trans. Power Electron.*, vol. 24, no. 12, pp. 2897–2906, Dec. 2009.
- [14] D. Yousfi, "Encoderless PM brushless drive for electric vehicle traction," in *Proc. IEEE IECON*, Nov. 2009, pp. 3797–3802.

- [15] A. Lidozzi, L. Solero, F. Crescimbeni, and A. Di Napoli, "SVM PMSM drive with low resolution Hall-effect sensors," *IEEE Trans. Power Electron.*, vol. 22, no. 1, pp. 282–290, Jan. 2007.
- [16] H. Kim, S. Yi, N. Kim, and R. D. Lorenz, "Using low resolution position sensors in bumpless position/speed estimation methods for low cost PMSM drives," in *Conf. Rec. IEEE IAS Annu. Meeting*, Oct. 2005, vol. 4, pp. 2518–2525.
- [17] Q. Zhu, Y. F. Shi, and D. Howe, "Rotor position sensing in brushless ac motors with self-shielding magnets using linear Hall sensors," *J. Appl. Phys.*, vol. 99, no. 8, pp. 08R 313–08R 313-3, Apr. 2006.
- [18] F. Caricchi, F. G. Capponi, F. Crescimbeni, and L. Solero, "Sinusoidal brushless drive with low-cost linear Hall effect position sensors," in *Proc. IEEE Power Electron. Spec. Conf.*, Jun. 2001, vol. 2, pp. 799–804.
- [19] R. Wegener, F. Senicar, C. Junge, and S. Soter, "Low cost position sensor for permanent magnet linear drive," in *Proc. IEEE PEDS*, Nov. 2007, pp. 1367–1371.
- [20] L. Xiao, Y. Yunyue, and Z. Zhuo, "Study of the linear Hall-effect sensors mounting position for PMLSM," in *Proc. IEEE ICIEA*, May 2007, pp. 1175–1178.
- [21] B. Widrow and D. Stearns, *Adaptive Signal Processing*. Englewood Cliffs, NJ: Prentice-Hall, 1985.
- [22] B. Widrow, J. R. Glover, Jr., J. M. McCool, J. Kaunitz, C. S. Williams, R. H. Hearn, J. R. Zeidler, E. Dong, Jr., and R. C. Goodlin, "Adaptive noise cancelling: Principles and applications," *Proc. IEEE*, vol. 63, no. 12, pp. 1692–1716, Dec. 1975.
- [23] J. Glover, "Adaptive noise canceling applied to sinusoidal interferences," *IEEE Trans. Acoust., Speech, Signal Process.*, vol. 25, no. 6, pp. 484–491, Dec. 1977.
- [24] M. Karimi-Ghartemani and A. K. Ziarani, "Periodic orbit analysis of two dynamical systems for electrical engineering applications," *J. Eng. Math.*, vol. 45, no. 2, pp. 135–154, Feb. 2003.
- [25] S. Luo and Z. Hou, "An adaptive detecting method for harmonic and reactive currents," *IEEE Trans. Ind. Electron.*, vol. 42, no. 1, pp. 85–89, Feb. 1995.
- [26] M. Karimi-Ghartemani and M. R. Iravani, "Measurement of harmonics/inter-harmonics of time-varying frequencies," *IEEE Trans. Power Del.*, vol. 20, no. 1, pp. 23–31, Jan. 2005.
- [27] D. Yazdani, A. Bakhshai, G. Joos, and M. Mojiri, "A real-time extraction of harmonic and reactive current in a nonlinear load for grid-connected converters," *IEEE Trans. Ind. Electron.*, vol. 56, no. 6, pp. 2185–2189, Jun. 2009.
- [28] R. E. Best, *Phase-Locked Loops: Design, Simulation, and Applications*. New York: McGraw-Hill, 2003.
- [29] R. Teodorescu *et al.*, "Power electronics for PV energy systems integration," in *Proc. IEEE Power Electron. Spec. Conf. Tutorial*, Jun. 2008, pp. 10–38.
- [30] L. Harnefors and H.-P. Nee, "A general algorithm for speed and position estimation of ac motors," *IEEE Trans. Ind. Electron.*, vol. 47, no. 1, pp. 77–83, Feb. 2000.
- [31] J. Jang, S.-K. Sul, J.-I. Ha, K. Ide, and M. Sawamura, "Sensorless drive of surface-mounted permanent-magnet motor by high-frequency signal injection based on magnetic saliency," *IEEE Trans. Ind. Appl.*, vol. 39, no. 4, pp. 1031–1039, Jul./Aug. 2003.



Sung-Yoon Jung (S'07) was born in Seoul, Korea, in 1979. He received the B.S. degree in electrical and electronic engineering from Hanyang University, Seoul, in 2005, and the M.S. degree in electrical engineering from the Pohang University of Science and Technology (POSTECH), Pohang, Korea, in 2008, where he is currently working toward the Ph.D. degree.

His research interests include the design, analysis, and control of power electronic systems, ac motor drive, and electric vehicle.



Kwanghee Nam (S'83–M'86) was born in Seoul, Korea, in 1956. He received the B.S. degree in chemical technology and the M.S. degree in control and instrumentation engineering from Seoul National University, Seoul, in 1980 and 1982, respectively, and the M.S. degree in mathematics and the Ph.D. degree in electrical engineering from the University of Texas, Austin, in 1986.

From 1998 to 2000, he was the Director of the Information Research Laboratories and the Dean of the Graduate School of Information Technology with the Pohang University of Science and Technology (POSTECH), Pohang, Korea, where he is currently a Professor in the Department of Electrical Engineering. His current research interests include ac motor control, power converters, motor design, and electric power train. He is the author of the book *AC Motor Control and Electrical Vehicle Applications* (Boca Raton, FL: CRC Press).